Rheol Acta (2008) 47:943–957
DOI 10.1007/s00397-008-0300-5

ORIGINAL CONTRIBUTION

A shear rheometer for measuring shear stress and both normal stress differences in polymer melts simultaneously: the MTR 25

Thomas Schweizer · Jürg Hostettler · Fredy Mettler

Received: 29 June 2007 / Accepted: 3 July 2008 / Published online: 8 August 2008

Abstract The MTR 25 is a multitask rheometer (for shear and squeeze flow) with 25 kg of normal force and a partitioned plate. Torque and normal force are measured at both, the inner disk and the outer ring of the plate. The first and second normal stress differences can be determined from a single test. The axial stiffness is high (10^7 N/m) by using rigid springs and strain gauges for the load cell. Monodisperse polystyrene (M_w = 206 kg/mol, 180°C) has been sheared in the range from 0.05 to 47 s^{-1}. The viscosity and first normal stress difference are highly reproducible. The second normal stress difference scatters and mirrors the instability at the rim. A critical comparison is made between the MTR 25 method and the single transducer evaluation method (RMS 800 method, Schweizer, Rheol Acta 41:337–344, 2002): Both yield excellent and coinciding viscosity and first normal stress difference data. The RMS 800 method gives more stable second normal stress difference data, since the normal force from the outer ring, which is influenced by edge fracture, is not used. Data for the RMS 800 method can be acquired on the MTR 25. The high normal force capacity permits larger samples and higher shear rates than on the RMS 800.

Keywords Rheometer · First normal stress difference · Second normal stress difference · Polymer melt · Edge fracture · Partitioned plate

Part of this paper has been presented at the 4th AERC in Naples, 2007.

T. Schweizer (✉) · J. Hostettler · F. Mettler
Department of Materials, Institute of Polymers,
ETH Zürich, 8093 Zurich, Switzerland
e-mail: thomas.schweizer@mat.ethz.ch

Introduction

Commercial rheometers which are suitable for nonlinear experiments (i.e., with precise temperature control, high normal force capacity, rigid construction) are still scarce on the market. Since the first paper on the Weissenberg Rheogoniometer was presented by Jobling and Roberts (1959), numerous efforts have been made to understand the flow of polymeric liquids and adapt the instruments accordingly. Meissner (1972) stated that axial stiffness was essential for correct normal force measurements. It was also observed that the time response due to gap opening is huge for small cone angles and spoils the normal stress data (Kaye et al. 1968; Meissner 1972). Hansen and Nazem (1975) analyzed this problem for a Newtonian fluid. There were numerous attempts to measure the second normal stress difference, as reviewed by Ohl and Gleissle (1992). Pollett (1955) was the first to fit a partitioned plate to his rheometer. Within resolution, he confirmed Weissenberg's hypothesis that $N_2 = 0$. It took quite a while until the idea was picked-up again and rendered to be practical by Meissner et al. (1989), taking the occasion of converting an RMS 800[1] from "hair dryer" heating to precise electric temperature control. So, it looked like everything was settled by the end of the 1980s and one knew how to correctly measure the full viscometric set of data. However, the principal motivation for the construction of the rheometer MTR 25 presented here came from the frustration to be always

[1] Rheometrics Mechanical Spectrometer, manufactured by Rheometric Scientific with a force rebalance transducer for torque and normal force (up to 20 N). Electrical heating fitted (Meissner et al. 1989).

limited in the size of the samples and the maximum shear rate, limitations set by the low normal force capacity of the RMS 800. The MTR 25 has deliberately been built as a robust machine for high loads, but with a limited resolution at low deformation rates.[2] The second motivation was to have a rheometer at hand with a partitioned plate for the one-sample determination of N_1 and N_2. The paper presents the first results of single-sample-determined N_1 and N_2 from this rheometer and compares them with the results obtained with the evaluation technique as used on the single transducer rheometer RMS 800. A particular focus is put on how edge fracture sets the limit of homogeneous flow and how this is expressed in the rheometric data and seen by surface particle tracking.

Experimental

Rheometer

The general set-up of the rheometer is shown in Fig. 1. The inner frame of the rheometer consists of two bearing plates, separated by two ground steel columns of 20 mm diameter. These keep the bearing plates at fixed distance and also guide the axial roller bearings for the moving member of the tool. The upper bearing plate carries the driving motor[3] with its gear box and the interchangeable cone with the diameter of 50 mm.

The tool is electrically heated and of the same design as on the RMS 800 (Meissner et al. 1989). Cones of angles 0.05, 0.1, and 0.15 rad are available. The lower member of the tool with the partitioned plate with an outer diameter of 50 mm sits on the crosshead. It is guided by axial roller bearings along the steel columns so that the cone and plate always remain coaxial. Attached to the crosshead are the load cells for the inner disk and for the outer ring. For sterical reasons, these cells are of different designs.

The one for the inner disk is shown in Fig. 2. To exclude any hysteresis from mounting stresses, the cage of the load cell is machined out of bulk machine steel. At three positions for the torque and three for the normal force, openings have been drilled and reamed to the crossbars of the cage. The inner disk of the partitioned plate (of radius R_i = 6, 8, or 10 mm) is attached to the base ring and the cell is mounted to the crosshead through the mounting ring. One force measuring element is shown in Fig. 3. It is a spring parallelogram and four strain gauges,[4] glued to the indicated positions, measure its deformation. The change in resistance is measured and amplified by digital am-

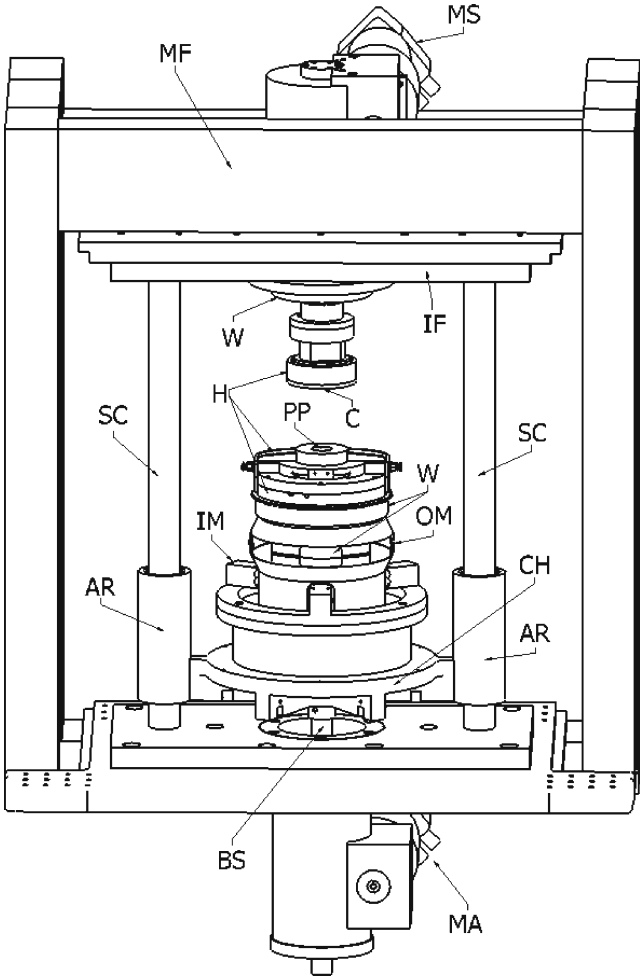

Fig. 1 Sketch of main components of rheometer. *MF* Main frame, carrying all periphery devices (sample loader, cleaning support for ring, cooling water rotameters, cooling water tempering, video camera), *IF* inner frame, *C* cone with drive and gear box, *CH* crosshead, *AR* axial roller bearing, *PP* partitioned plate, *MA* motor for axial displacement, *MS* motor for shearing, *BS* ball screw for axial displacement, *H* electrical heating, *W* water cooling, *IM* inner load cell, *OM* outer load cell, *SC* ground and polished steel columns

[2]The design of a low load rheometer is equally challenging. Since normal forces decrease quadratically with rate, the temperature must be well controlled to get a perfectly stable baseline. Such requirements can only be obtained with electrically temperature control, but not with convection ovens. The ARES, e.g., can keep temperature constant within ±0.05°C at a level of 200°C, which is far too noisy to even explore the full range of its force rebalance transducer.

[3]Maxon EC motor, Type 276575 with tacho generator.

[4]Manufacturer HBM, Type 1-LC11-3/350, resistance 350 Ω each.

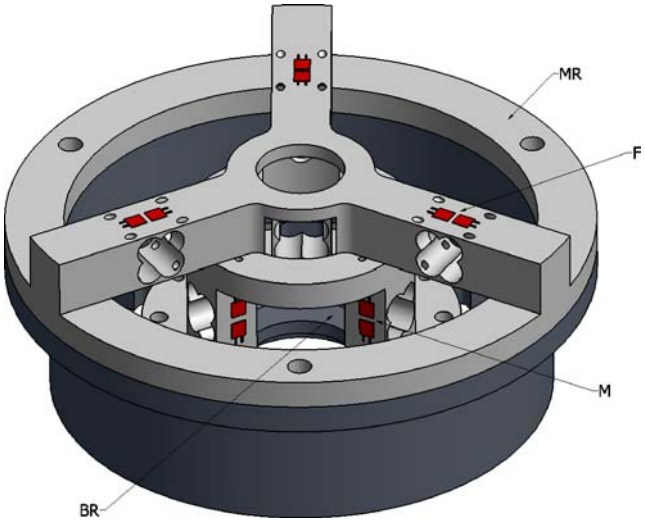

Fig. 2 Sketch of inner load cell. *F* Normal force spring element, *M* torque spring element, *MR* mounting ring, *BR* base ring

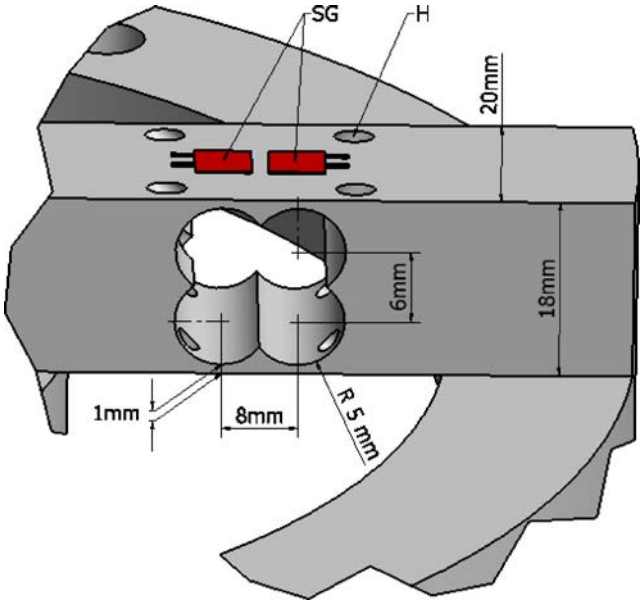

Fig. 3 Sketch of normal force spring element F from Fig. 2. *SG* Upper strain gauges (lower ones not shown), *H* holes for wire feed through

plifiers.[5] To double the measured signal, the four strain gauges are combined in a Wheatstone bridge.

The load cell for the outer ring is shown in Fig. 4. It is of a barrel shape with openings milled to the periphery. The barrel shape has been chosen to induce a bending moment to the wings, when the ring carries a normal load. The wings are also sheared when a torque acts on the cell. But since the wall thickness is 1 mm, the shear sensitivity is not very high (see Table 1). There are three rectangular wings for the normal force and three H-shaped wings for torque measurement. The normal force wings are fitted with the same type of strain gauges as the inner load cell; the torque wings carry special fishbone-type gauges.[6]

The main motivation for using strain gauges is their supreme sensitivity. This allows using quite robust springs (see Fig. 3) which prevents accidental over-straining of the load cell. The wings in Fig. 4 have a thickness of 1 mm. Since the tools are electrically heatable to 220°C, locations marked by W in Fig. 1 are water-cooled. This prevents heating-up and warping of the inner frame and also keeps the load cells at a constant temperature of 30°C. Tempering of the cooling water is essential for avoiding any condensation of atmospheric humidity on the strain gauges. Figure 4 also shows the handle to easily remove the outer ring for cleaning. Since disconnection of the heating power is not allowed, there is a cleaning support attached to the main frame of the rheometer. The outer ring is adjustable so that at each temperature, it can be set to the same height as the inner disk. The ring gap to the inner disk is 0.05 mm wide. During operation, the handle of the ring and the load cells are protected by a bell-shaped hood (not shown), so that crumbs from brush cleaning do not fall in.

Since the load cells are based on the measurement of spring deflections, they have to be calibrated.

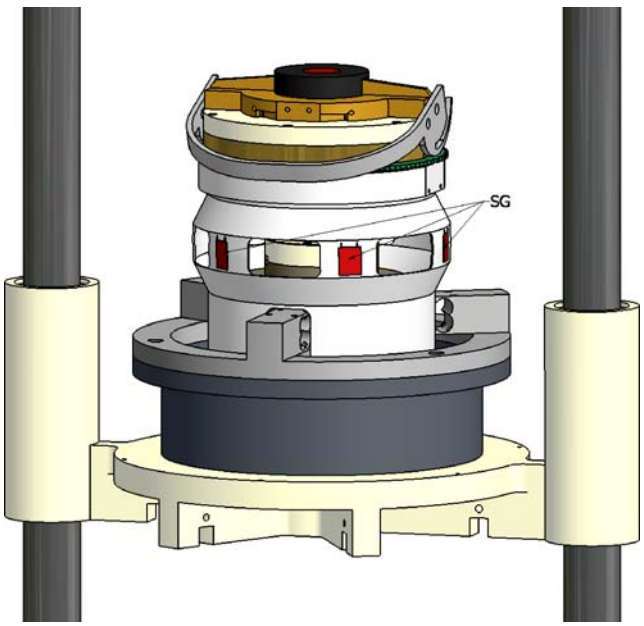

Fig. 4 Outer load cell. *SG* Strain gauges

[5]MGCplus AB22A from Hottinger Baldwin Messtechnik, Darmstadt, Germany.

[6]Manufacturer HBM, Type 1-XG21-6/350, resistance 350 Ω each.

Table 1 Physical specifications of rheometer MTR 25

Parameter	Value	Unit
Temperature	25–220	°C
Long time stability	0.01	°C
Min. angular velocity	$2.36 \cdot 10^{-3}$	rad/s
Max. angular velocity	7.076	rad/s
Min. shear rate with $\alpha = 0.15$ rad	$1.6 \cdot 10^{-2}$	s^{-1}
Max. shear rate with $\alpha = 0.15$ rad	47.2	s^{-1}
Min. crosshead travel speed	$2.57 \cdot 10^{-4}$	mm/s
Max. crosshead travel speed	0.772	mm/s
Axial stiffness K_A	10^7	N/m
Tool acceleration time, without overshoot to max. speed	50	ms
Data acquisition rate	75	Hz
Max. inner torque	1,300	mN m
Signal resolution[a], inner disk torque M_i	0.174	mN m
Signal resolution[a], outer ring torque M_o	1.5261	mN m
Max. inner force	250	N
Signal resolution[a], inner disk force F_i	4.36	mN
Signal resolution[a], outer ring force F_o	14.62	mN

[a]Determined as the standard deviation from averaging 200 data points with $R_i = 6$ mm at $T = 180$°C

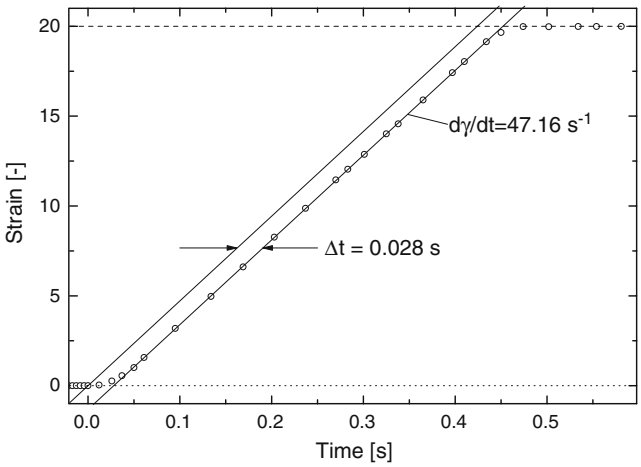

Fig. 5 Effective motion of motor during start-up with $\dot{\gamma} = 47.16\,s^{-1}$ and relaxation at $\gamma = 20$ with $\alpha = 0.15$ rad (maximal motor speed 3,000 rpm). The inclined lines correspond to a constant shear rate of $\dot{\gamma} = 47.16\,s^{-1}$. The time to reach this constant rate is about 50 ms. The time shift Δt of 28 ms depends linearly on motor speed and was corrected in the data shown in Figs. 6–8

Appropriate calibration tools have been manufactured to apply torque and normal load to the inner and outer load cells. Care has been taken that the normal force is applied in the proper direction, not in the wrong one, as e.g., in the calibration of the ARES.[7]

Drive

The control of the rheometer is by software written in Labview[8] and a touch screen interface. The temperature is read from Pt 100 sensors with the same digital amplifiers as for the strain gauges and kept constant by an SPS controller. The motors for shear and axial displacement are speed-controlled. The rotation speed is detected from a tacho generator with a resolution of 2,000 pulses per revolution.

The performance of the shear drive is shown in Fig. 5. The symbols are the effective strain as measured at the motor axis by the tacho generator. The bold line through the linear part of the symbols has a slope of 47.16 s^{-1}, corresponding to full motor speed with the 0.15 rad cone. The dashed line is the set strain. Due to the acceleration time, there is a time delay Δt between the two bold lines:

$$\Delta t = 5.86 \cdot 10^{-4}\,\dot{\gamma}\ [s] \qquad (1)$$

This time delay was corrected since, though small, it shows up as considerable deviations in the log–log plots in Figs. 6, 7, 8.

Material

The samples of monodisperse polystyrene PS 206k were made by vacuum-melting tablets pressed at room temperature from precipitated PS powder. Details can

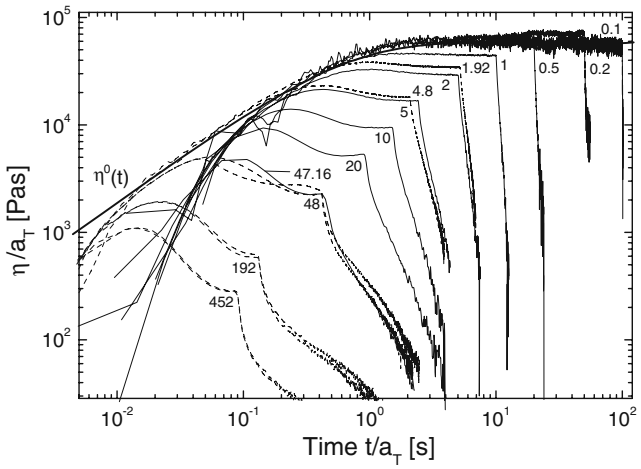

Fig. 6 Start-up viscosity η/a_T. *Solid lines* PS 206k at 180°C. *Dashed lines* Data shifted from 160°C. Common test conditions: $\alpha = 0.15$ rad, $R_i = 6$ mm. The time for all tests is corrected by $t = \left(t_{meas.} - 5.86 \cdot 10^{-4} \cdot \dot{\gamma}_{meas.}\right)/a_T$. $\dot{\gamma}_{meas.}$ is the shear rate at the measuring temperature. *Numbers in the graph* are the shear rates at 180°C in [s^{-1}]. The bold curve is $\eta^0(t)$ calculated from the RTS

[7]ARES LR2, manufactured by TA Instruments, Eschborn, Germany, with a force rebalance transducer and a maximal normal force of 20 N. Temperature control by a convection oven

[8]Registered Mark, version 7.1

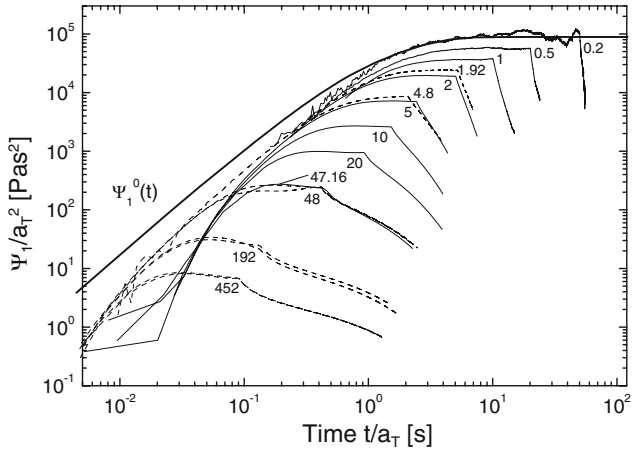

Fig. 7 First normal stress coefficient Ψ_1/α_T^2. *Solid lines* PS 206k at 180°C. *Dashed lines* Data shifted from 160°C. The time for all tests is corrected by $t = \left(t_{\text{meas.}} - 5.86 \cdot 10^{-4} \cdot \dot{\gamma}_{\text{meas.}}\right)/a_T$. No correction made for compliance. The bold curve is $\Psi_1^0(t)$ calculated from the RTS

be found in Schweizer (2004). The physical properties of the material are summarized in Table 2, and the linear relaxation time spectrum (RTS) at the reference temperature of 180°C in Table 3. The approximate radii R of the samples at measuring temperature were: 9.1 mm at 160°C, 12.5 mm at 170°C, and 10.1–18 mm at 180°C. Experiments at 170°C were performed to examine the low shear rate regime, the ones at 160°C to check whether time–temperature superposition is applicable to non-linear shear tests.

The linear relaxation time spectrum in Table 3 is used for calculating η_0 and $\Psi_{1,0}$ in Table 2 and the time-dependent $\eta^0(t)$ and $\Psi_1^0(t)$ envelops in Figs. 6, 7, 11, and 12.

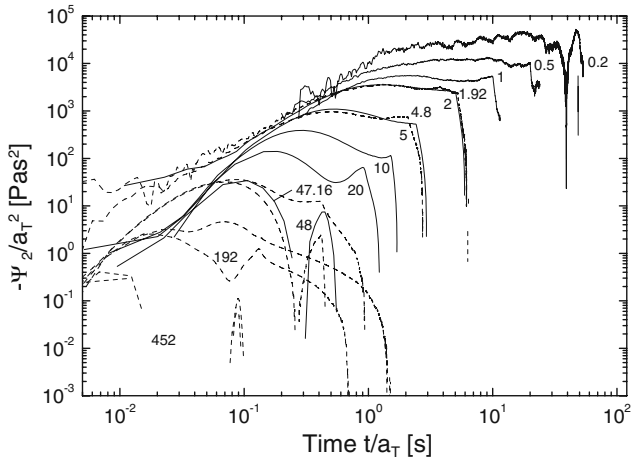

Fig. 8 Second normal stress coefficient $-\Psi_2/\alpha_T^2$. *Solid lines* PS 206k at 180°C. *Dashed lines* Data shifted from 160°C. The time for all tests is corrected by $t = \left(t_{\text{meas.}} - 5.86 \cdot 10^{-4} \cdot \dot{\gamma}_{\text{meas.}}\right)/a_T$

Table 2 Physical properties of materials used in this study

Property	PS 206k	PS 158K
Supplier	G. Kisker, Steinfurt, Germany	BASF
Lot Nr.	GKps200k	9 534 574
M_w [kg/mol]	206	336
M_w/M_n [-]	1.06	2.85
M_e [kg/mol]	13[a]	13[a]
$Z = M_w/M_e$ [-]	15.8	25.8
T_{meas} [°C]	180	190
ρ at T_{meas} [g/cm^3]	0.983	0.978
a_T 160→180°C	9.6	
η_0 at T_{meas} [Pa s]	58,600	44,500
$\Psi_{1,0}$ at T_{meas} [Pa s^2]	89,100	124,600
τ_d [s]	0.76	1.4
$\tau_R = \tau_d/3Z$ [s]	0.016	0.018

[a] Atactic polystyrene, from Fetters et al. (1999)

Working equations

The outer working radius R of the sample is calculated from its mass m with Eq. 2, assuming a spherical shape of the surface of the loaded molten sample.

$$R = \sqrt[3]{\frac{3m}{2\pi\rho\alpha}} \quad \text{Radius of sample} \tag{2}$$

$$N_i = \frac{2F_i}{\pi R_i^2} \quad \text{Normal stress on inner disk} \tag{3}$$

$$F = F_i + F_o \quad \text{Total normal force} \tag{4}$$

The first normal stress difference is calculated from Eq. 5. Adams and Lodge (1964) have derived this relation under the assumption that the surface is part of a sphere.

$$N_1 = \frac{2F}{\pi R^2} \quad \text{First normal stress difference} \tag{5}$$

Table 3 Relaxation time spectrum (RTS) of PS 206k at 180°C, calculated with the IRIS program, version 8.0, Winter (1997)

τ_i[s]	g_i [Pa]
2.73E-06	4,547,000
3.27E-05	448,700
0.000323	132,900
0.004186	61,020
0.04115	63,540
0.344897	79,700
1.234232	22,800

If this expression is inserted into Eq. 6 (Meissner et al. 1989), one can solve for N_2 and gets Eq. 7 for the second normal stress difference.

$$N_i = \frac{2F_i}{\pi R_i^2} = N_1 + 2 \cdot (N_1 + 2 \cdot N_2) \ln\left(\frac{R}{R_i}\right) \tag{6}$$

$$N_2 = \frac{1}{2\pi R^2}\left[\frac{F_i\left(\frac{R}{R_i}\right)^2 - F}{\ln\left(\frac{R}{R_i}\right)} - 2F\right] \tag{7}$$

Since for the cone–plate geometry the shear stress is constant throughout the gap, the torques acting on outer ring and inner disk can be obtained by simple integration. Thus, the following equations hold which yield the same stress for the two partitions of the plate, as long as the flow is homogeneous and the edge is not fracturing:

$$p_{21,i} = \frac{3M_i}{2\pi}\frac{1}{R_i^3} \quad \text{Shear stress inner disk} \tag{8}$$

$$p_{21,o} = \frac{3M_o}{2\pi}\frac{1}{\left(R^3 - R_i^3\right)} \quad \text{Shear stress outer ring} \tag{9}$$

$$\frac{R}{R_i} = \sqrt[3]{\frac{M_o}{M_i} + 1} \tag{10}$$

In Eqs. 2–10: m is the mass of the sample, α the cone angle, ρ the material density at test temperature, R_i radius of the inner disk, F_i force on the inner disk, F_o force on the outer ring, M_i torque on the inner disk, and M_o torque on the outer ring.

If a sample of unknown density is to be measured, Eq. 2 cannot be applied. Instead, if the flow is homogeneous and the edge smooth, Eq. 10 allows calculating R from the two torques.

Loading of the sample

Working with polymer melts without entirely filling the gap always involves the problem to centrically place a cylindrical sample on the heated flat member of the tool. In our other rheometers ARES and MCR 300,[9] we use centering gauges for each tablet diameter. For the MTR 25, a diameter-independent loading system has been developed. The sample is placed on an auxiliary table and centered by means of an optical lamella aperture. Then, the tablet is transferred from this position to the center of the hot plate by a vacuum suction system pivoting around the right column steel columns in Fig. 1. Room temperature melts and polymer solutions have to be solidified first or loaded by another procedure.

Preliminary experiments have shown that N_2 depends on the conditioning of the rim of the sample, i.e., its curvature. This finding is corroborated by a theoretical study by Venerus (2007). After loading a tablet and penetrating the cone, the melt is bulged to a radius $r_c = \alpha R$ (Schweizer and Stöckli 2008). For the worst case, when one started the test immediately with this bulge, Venerus calculated that the error in N_1 is 13% and the one in $-N_2/N_1$ still 11%. Thus, the need for shaping the rim closer to a sphere is obvious. The evolution of the curvature of the rim and its effect on viscosity and N_1 has been quantified by Schweizer and Stöckli (2008) as a function of time and temperature for the same polystyrenes as used in this study. According to this study, the time required to obtain the ideal spherical shape is unrealistically long. As a compromise between a practical conditioning time and some smoothing of the surface, the following loading procedure was applied at constant temperature of 180°C:

- Note: The truncation for the 0.15 rad cone is 0.076 mm.
- The sample is loaded to a gap of 0.026 mm (to increase the wetting radius).
- The normal force on the inner disk is allowed to relax to 1 N.
- The gap is opened to 0.076 mm.
- After a conditioning time of 20 min, the test is started.

For practical reasons, this procedure was also applied at 160 and 170°C. This means that the effective time for conditioning the rim was only 2 min compared to 180°C, but a corresponding waiting time of 200 min prior to each test was not found practical.

Results and discussion

Step shear rate experiments

Tests have been performed in the range $0.05 < \dot{\gamma} < 47.16\ s^{-1}$ at 180°C and $0.2 < \dot{\gamma} < 47.16\ s^{-1}$ at 160°C, corresponding to $1.92 < \dot{\gamma} < 452\ s^{-1}$ at 180°C. In order to explore the low shear rate regime, tests with large ($R = 12.5$ mm) samples have been performed at 170°C in the range $0.02 < \dot{\gamma} < 0.4\ s^{-1}$, corresponding to

[9] Manufactured by Anton Paar, Ostfildern, Germany, with directly electrically heated plate and radiation heating for the cone.

Table 4 Advantages and disadvantages for performing tests at lower temperatures

Parameter	Standard test temperature (180°C)	Low test temperature (160°C) with shifting to reference temperature (180°C)
After loading: rest time for shaping edge toward sphere	15–30 min	Several hours
Shear rate (s^{-1})	Up to 47	Up to 450
Acceleration time	~Shear rate (Eq. 1)	Negligible
Tests limited by transducer	Only at low shear rate	Only at low shear rate
Test limited by adhesion	No	Possible
Data acquisition rate (Hz)	75	720

The shift factor $a_T = 9.6$ is for polystyrene.

$0.056 < \dot{\gamma} < 1.12\ s^{-1}$ at 180°C. The common settings on the MTR 25 were a cone angle α of 0.15 rad and a radius of the inner disk R_i of 6 mm, except for the results in Figs. 11, 12 and 13. All results are reported for a reference temperature of 180°C.

For tests performed at lower temperature, the resolution on the time axis is increased by a factor of a_T. Is it therefore meaningful to generally perform tests at lower temperatures? There is no unambiguous answer to this question. The arguments are compared in Table 4.

Actually, everything is in favor of low test temperatures, except for the first point. Starting the test from a well-shaped rim is crucial for N_2 measurements. According to Schweizer and Stöckli (2008), aiming at a spherical shape of the rim (PS 206k, 180°C, α = 0.15 rad, R = 10.1 mm) takes about 160 min. Even if one admits half of that time because it is a conservative limit, it is still too long for screening many samples. If one therefore uses a shorter conditioning time, it is important to keep it strictly constant because otherwise one observes increased scattering of the data, in particular of N_2.

Figures 6 and 7 show the time-dependent shear viscosity η and the first normal stress coefficient Ψ_1. As envelops to the different experiments, $\eta^0(t)$ and $\Psi_1^0(t)$ are drawn, both calculated from the RTS in Table 3 with the following equations:

$$\eta^0(t) = \int_0^\infty H(\tau)\left(1 - \exp\left(-\frac{t}{\tau}\right)\right) d\tau \tag{11}$$

$$\Psi_1^0(t) = 2\int_0^\infty H(\tau)\tau\left\{1 - \left(1 + \frac{t}{\tau}\right)\exp\left(-\frac{t}{\tau}\right)\right\} d\tau \tag{12}$$

The partitioned plate technique is particularly suitable for very reproducible viscosity data, if only the torque from the inner disk is evaluated and thus any instability from the rim screened (Schweizer 2004). This is why for the viscosity curves in Fig. 6, there is fair agreement between data measured at 160 and 180°C. The different short time behavior ($t < 0.2$ s) originates from the tool acceleration times of 0.05 s at 180°C and 0.005 s at 160°C.

The first and second normal stress coefficients are shown in Figs. 7 and 8. With the RMS 800 method, only the normal force measured at the inner disk is evaluated, i.e., the part of the sample less affected by edge instabilities (Schweizer 2002). In return, several repetitive runs have to be performed for one experiment. The MTR 25, in addition, also measures the force on the outer ring F_o, which depends much more on the shape of the rim[10] and edge fracture. This is why the N_2 data measured at the MTR 25 are very sensitive to the latter. The Ψ_2 data in Fig. 8 does not look very reproducible and shows some scattering. In contrast, Ψ_1 in Fig. 7 is very consistent and reproducible. These facts show that Ψ_2 is a parameter quantifying the stress in the very surface of the sample which is heavily disrupted for rates $\dot{\gamma} > 10\,s^{-1}$ and strains $\gamma > 10$. Ψ_1 on the other hand acts perpendicular to the plates and gets its largest contribution from the inner part of the sample less affected by edge fracture. The steady-state values of η and the two normal stress coefficients are shown in Fig. 9.

The ratio $\Psi = -N_2/N_1$ of the two normal stresses displayed in Fig. 10 shows shear thinning behavior. The slope of a power law fit is not clear from first sight. However, in Fig. 9, power laws can be fitted to Ψ_1 and Ψ_2, with slopes given in Table 5. From this, a slope of −0.37 results for $\log\Psi$ vs. $\log\dot{\gamma}$. This value is smaller than the −0.5 predicted by the Doi–Edward and Giesekus theories. The comparison with other data in Table 5, however, shows that experimental findings are closer to −1/3 than to −0.5. The slope of −0.48 for

[10] A direct implication for the experiments is that for the signal F_o to be strong enough, the sample radius R should be typically $R > 1.25 \cdot R_i$. For the RMS 800 method (considering F_i only), this restriction does not exist.

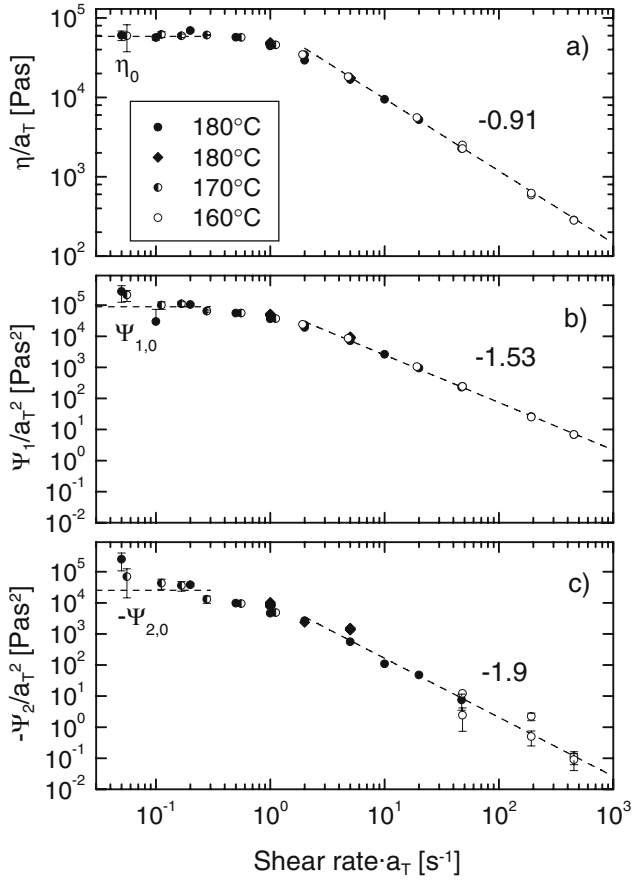

Fig. 9 Steady-state values of η (**a**), Ψ_1 (**b**), and $-\Psi_2$ (**c**) at 180°C. Measuring temperatures as indicated in the legend. *Numbers* are the slope of a power law fit in the range $\dot{\gamma} > 2\,s^{-1}$. $\eta_0 = 58.6$ kPa s, $\Psi_{1,0} = 89.1$ kPa s^2. $-\Psi_{2,0} = 25.5$ kPa s^2 is drawn in **c**, such that $-\Psi_{2,0}/\Psi_{1,0} = 2/7$. ♦ is data measured at 1 and 5 s^{-1} with prolonged conditioning time of 40 min instead of 20 min prior to start

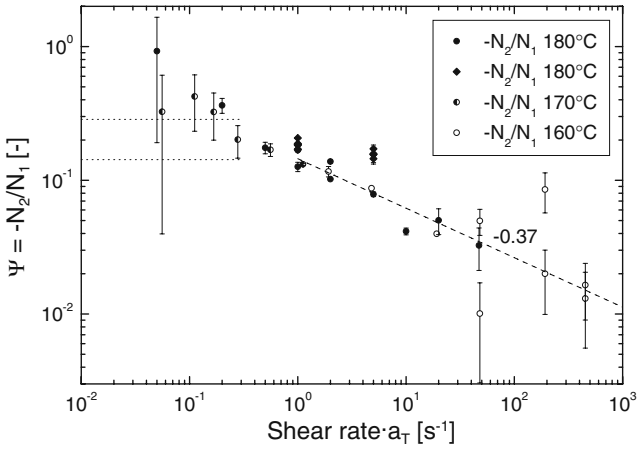

Fig. 10 Normal stress ratio $\Psi = -N_2/N_1$. -0.37 is the slope of the *dashed line*. The *horizontal dotted lines* are the low shear rate limits 1/7 and 2/7 predicted by the Doi–Edwards theory with and without independent alignment approximation. ♦ symbol: see legend of Fig. 9

PS 158K is clearly higher, but this could be due to its polydispersity.

Table 5 reveals that shear rate-dependent data on $|N_2|$ are still scarce. In Schweizer (2002), N_2 data is very crude, so that no shear rate dependence can be given. The data were measured at the RMS 800 up to 30 s^{-1}. Because of the 2 kg limit, the smallest inner disk ($R_i = 4$ mm) and small samples (transducer overload for $R > 6.5$ mm) have to be used for this rate. Together with the inherent trend of the monodisperse melt to flow inhomogeneously, measurements were done at the limit of the possible. That is why a comparison with the MTR 25 can only be made for curves modeled to the RMS 800 data (MLD and TCR in Table 5).

The low shear rate data in Fig. 10 show a trend toward $\Psi > 2/7$. This is not a violation of the Doi–Edward theory, but a result of the minor normal force signals. In particular, the outer force F_o becomes very noisy. Besides the short time noise as given in Table 1, there is also a long time drift in the baseline (order 0.05 N), possibly because the outer load cell is not as precisely thermostatized as the inner one. Up to now, no series of measurements with different R has been performed on the MTR 25 at a low rate, allowing the evaluation of Ψ with the RMS 800 method.

In Figs. 9 and 10, the symbol ♦ refers to measurements done recently at 180°C with the knowledge of shear banding (Schweizer and Stöckli 2008), i.e., with a prolonged conditioning time of 40 min instead of 20 min. The result is that η is unchanged, N_1 slightly, but N_2 and Ψ clearly higher than the data from the first group of measurements with 20 min of rest time. Because of this strong dependence, it is important that the conditioning time is strictly kept constant within a series of experiments. The effect of the conditioning time on the magnitude of N_1 is discussed in Schweizer and Stöckli (2008). For N_2, this dependence needs to be studied in more detail.

Comparison of two methods to evaluate N_1 and N_2

The RMS 800 used so far is equipped with a single transducer, reading torque and normal force from the inner disk. The evaluation procedure (termed RMS 800 method) for obtaining N_1 and N_2 through Eq. 6 is described in Schweizer (2002).

In this paragraph, we compare the results obtained with the RMS 800 method and the MTR 25 method (Eqs. 4, 5, and 7) from raw data acquired with the MTR 25. Sample radii in the range $10 < R < 18$ mm and two

Table 5 Predictions by different theories and literature values for the shear rate dependence of the indicated quantities in the power law regime

Source	dlog η/dlog $\dot{\gamma}$	dlog Ψ_1/dlog $\dot{\gamma}$	dlog $\lvert\Psi_2\rvert$/dlog $\dot{\gamma}$	dlog Ψ/dlog $\dot{\gamma}$
PS 206k melt, this work	-0.91 ± 0.02	-1.53 ± 0.02	-1.9 ± 0.08	-0.37 ± 0.06
Doi–Edward[a]		-2	-2.5	-0.5
Giesekus[a]		-1.5	-2	-0.5
MLD, $\delta_2 = 1$[b]	-0.89 ± 0.01	-1.46 ± 0.02	-1.76 ± 0.02	-0.3 ± 0.01
TCR, $\delta_2 = 0$[b]	-1.48 ± 0.04	-1.72 ± 0.03	-2.01 ± 0.03	-0.29 ± 0.01
PS 200k melt[b]	-0.88 ± 0.02	-1.53 ± 0.1	n.d.	n.d.
PS solution, Magda and Baek (1994)				-0.31 ± 0.06
PS solution, Kalogrianitis and van Egmond (1997)				-0.37 ± 0.05
PS 158K melt, Schweizer (2002)	-0.75 ± 0.1	-1.37 ± 0.09	-1.85 ± 0.06	-0.48 ± 0.04

n.d. Not determined
[a] As cited in Kalogrianitis and van Egmond (1997)
[b] *MLD* Mead–Larson–Doi theory, *TCR* thermodynamically consistent reptation model. δ_2 convective constraint release parameter. See Schweizer et al. (2004) for details

diameters of the inner disk (R_i = 6 and 10 mm) have been used in the acquisition of these data. Figure 11 shows viscosities for two shear rates of 1 and 5 s^{-1} and Fig. 12 the corresponding normal stress coefficients.

RMS 800 method: torque and normal force from inner disk

Figure 11a and c shows excellent viscosity data up to $\gamma = 30$ ($\dot{\gamma} = 1\,s^{-1}$) and $\gamma = 20$ ($\dot{\gamma} = 5\,s^{-1}$). After the overshoot, the viscosity is constant and the reproducibility within 4% to 10%. This is one motivation for using the partitioned plate technique for precise viscosity measurements (see Schweizer 2004).

In Fig. 12, the open circles with error bars show Ψ_1 and $|\Psi_2|$ evaluated with the RMS 800 method from the normal forces of the inner disk F_i. Figure 13 shows exemplarily how the normal stress coefficients are determined from the normalized inner force (N_i, Eq. 3) at a strain of 10. Both sets of N_i for R_i = 6 and 10 mm show the same linear dependence on $\ln(R/R_i)$ as requested by Eq. 6. N_1 is the y-intercept of the linear

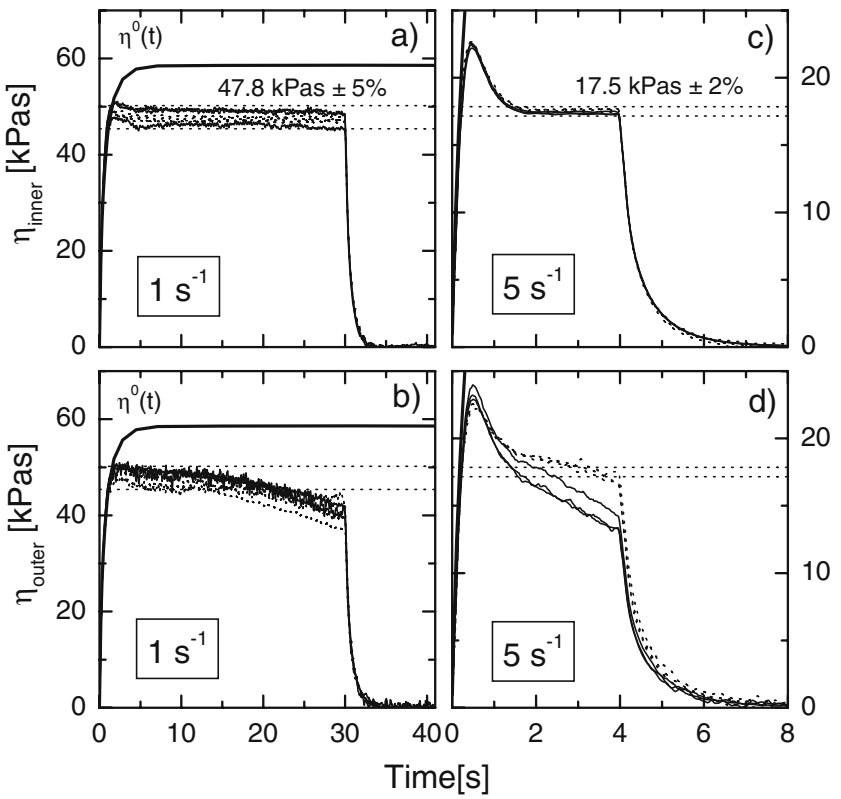

Fig. 11 Time-dependent viscosities for the samples shown in Fig. 13, measured at the inner disk (**a** and **c**) and the outer ring (**b** and **d**). *Solid lines* R_i = 10 mm, *dotted lines* R_i = 6 mm. The *bold lines* are $\eta^0(t)$ calculated from the RTS. The *dotted horizontal lines* show the average steady-state viscosity η_{ss} with the uncertainty given

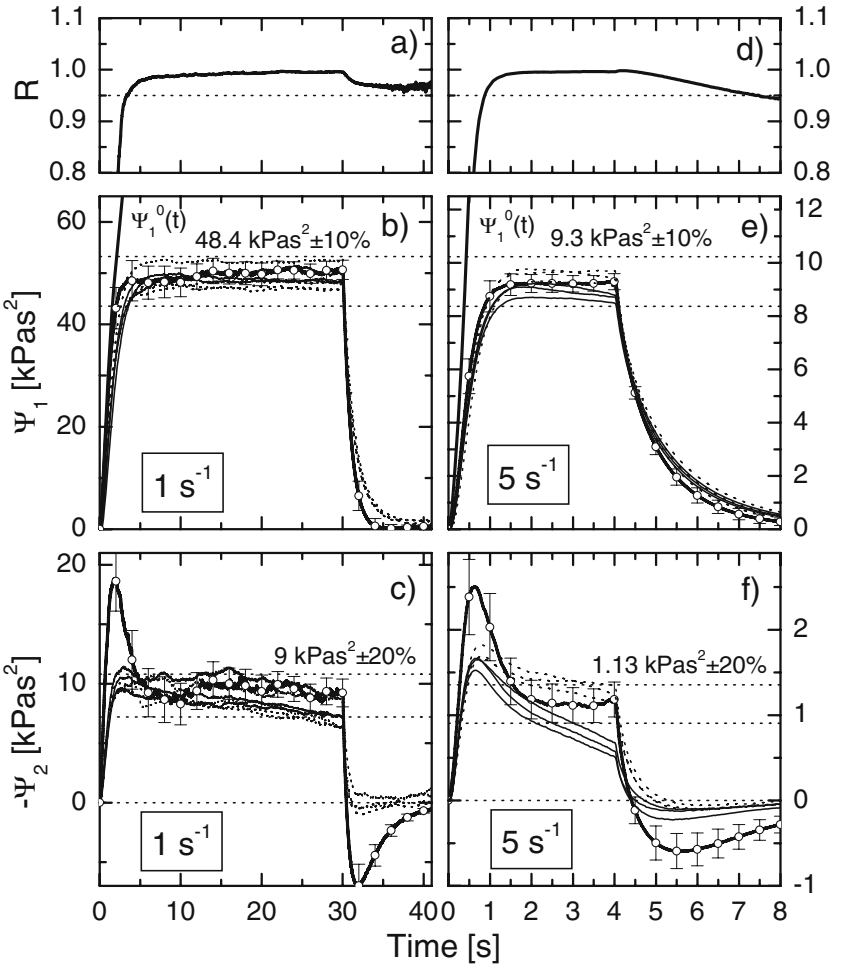

Fig. 12 **b–c**, **e–f** Time-dependent normal stress coefficients for the samples shown in Fig. 13, determined with the RMS 800 method (*open circles with error bars*) and the MTR 25 method (*bold lines* R_i = 10 mm, *dotted lines* R_i = 6 mm). **a**, **d** Regression coefficient R of the linear regression N_i vs. $\ln(R/R_i)$ for the RMS 800 method as shown in Fig. 13. The *bold lines* in **b** and **e** are $\Psi_1^0(t)$ calculated from the RTS. The *dotted horizontal lines* show the average steady-state values of Ψ_1 and $|\Psi_2|$ at about $\gamma = 10$ with the uncertainty given

fit; N_2 is extracted from its slope. Figure 12a and d shows the regression coefficient R for the linear fit. The regression quality increases markedly for $\gamma \gtrsim 3$. For $\dot{\gamma} = 1\,s^{-1}$: $R > 0.8$ for $\gamma > 2.25$ and $R > 0.95$ for $\gamma > 3.5$ and for $\dot{\gamma} = 5\,s^{-1}$: $R > 0.8$ for $\gamma > 3$ and $R > 0.95$ for $\gamma > 4.4$. Beyond $\gamma \gtrsim 4$ far into the relaxation part of the experiment, R is larger than 0.95. Therefore, the steady-state values of N_1 and N_2 obtained with the RMS 800 method are correct.

The reason for the failure of the RMS 800 method at $\gamma \gtrsim 3$ is that transient normal force signals of samples with different size R have to be correlated. They are very sensitive to small changes in the starting conditions, i.e., the shape of the sample's rim. The overshoot of N_2 is in this critical zone and calculated much larger than with the MTR 25 method. The same observation was made by Schweizer et al. (2004) in a comparison of the RMS 800 data with simulations.

Interestingly, a similar discrepancy can also be observed after cessation of steady flow: $|\Psi_2|$ shows a sign change and a strong undershoot, an effect being much less pronounced for the curves calculated with the MTR 25 method. But contrary to the start-up, the correlation R of the linear fit is excellent with $R > 0.95$ for both shear rates although Figs. 11b, d and 16 show that the flow is by far no longer homogeneous.

MTR 25 method: torque and normal force from the inner disk and the outer ring

Contrary to the normal stress coefficients, the viscosities can be evaluated independently for the two partitions. The inner torque gives good viscosity data, since the radius R_i is mechanically defined and constant, and there is no free surface to fracture. The outer torque, however, monitors every change in sample geometry. If the sample radius decreases due to edge fracture or dewetting, the torque will reduce in magnitude. This is seen in Fig. 11b and d. For $\dot{\gamma} = 1\,s^{-1}$, there is a steady state up to about $\gamma \approx 12$. For $\dot{\gamma} = 5\,s^{-1}$, the well-defined geometry is already lost in the descent from

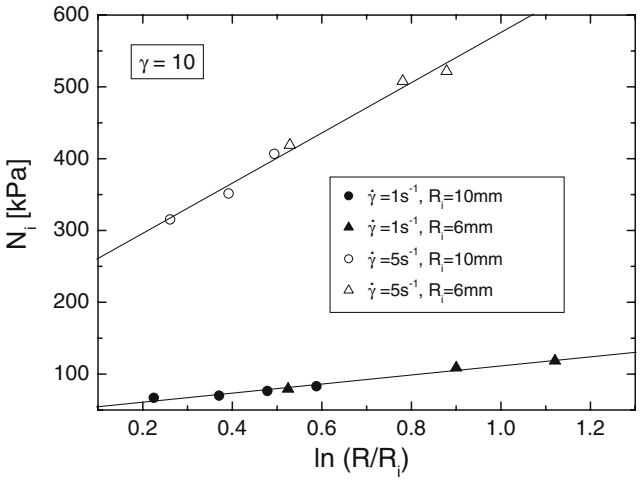

Fig. 13 Determination of N_1 and $|N_2|$ with the RMS 800 method. Values of N_i (Eq. 3) at $\gamma = 10$ from 7 ($\dot{\gamma} = 1\,\mathrm{s}^{-1}$) or 6 ($\dot{\gamma} = 5\,\mathrm{s}^{-1}$) repetitive tests with samples of different sizes. N_1 is the y-intercept, $N_2 = 0.25 \cdot \text{slope} - 0.5 \cdot N_1$. This linear regression has to be repeated for every time step to get $N_1(t)$ and $|N_2|(t)$

the overshoot and there is no steady state. There is a separation by the radius of the inner disk R_i: For the larger ($R_i = 10$ mm), the outer tool probes a ring of sample of width $3 < (R - R_i) < 4.4$ mm, essentially only its rim. For the $R_i = 6$ mm disk, these values are $7 < (R - R_i) < 8.4$ mm, i.e., the outer ring also probes part of the sample not affected by edge fracture, as evidenced in Fig. 11a and c.

The discussion above has shown that a fracturing edge expresses in a decrease of the torque measured at the outer ring. Since N_2 acts on the sample's rim, an even stronger dependence is expected. Figure 12f indeed shows that the sets of curves for $R_i = 6$ and 10 mm are quite different: The decrease of $|\Psi_2|$ with time is much stronger for $R_i = 10$ mm. For the Ψ_1 data in Fig. 12e, this distinction can also be made, but is much less pronounced so that the curves almost coincide with the data evaluated with the RMS 800 method. For $\dot{\gamma} = 1\,\mathrm{s}^{-1}$, the coincidence for the two methods is even better up to a strain of ≈12.

Rheometer compliance

An important feature to check is whether the relaxation time (τ_1^-) after cessation of flow is independent of sample size. Otherwise, one would actually sense the compliance of the rheometer and not the relaxation properties of the melt, as discussed by Schweizer and Bardow (2006). Figure 14 shows that the axial response time t_a

$$t_\mathrm{a} = \frac{6\pi R\eta}{K_\mathrm{A}\alpha^3} \quad \text{with } K_\mathrm{A} = 10^7 \mathrm{N/m} \tag{13}$$

changes by roughly 0.5 s for the range of sample radii studied. There is a clear but minor trend for $(\tau_1^-)_{N_1}$ to rise with t_a, in particular for $\dot{\gamma} = 1\,\mathrm{s}^{-1}$. Within scatter, $(\tau_1^-)_{p_{21}}$ and $(\tau_1^-)_{N_2}$ are both independent of t_a. The observation that $|N_2|$ relaxes faster than the other stresses can be explained either by the fact that constraints at the surface relax much quicker than those in the bulk or by shear banding, altering considerably the surface

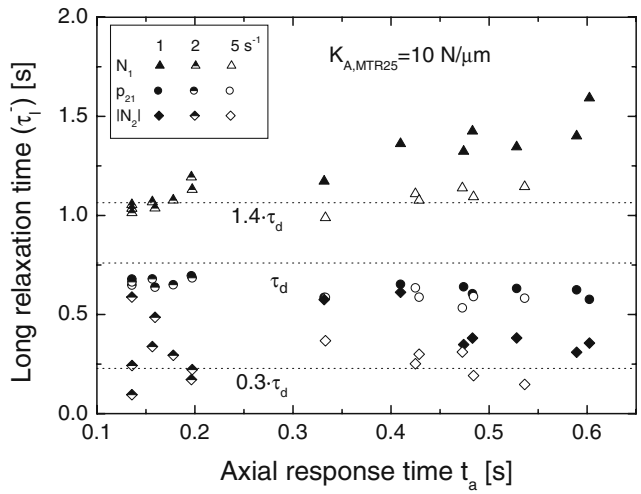

Fig. 14 Long relaxation times (τ_1^-) measured in the time window $0.5 < t' < 0.7$ s as a function of the axial response time t_a (proportional to sample size, Eq. 13). Time t' starts when the flow stops. Data are given for three shear rates, as shown in the matrix in the legend

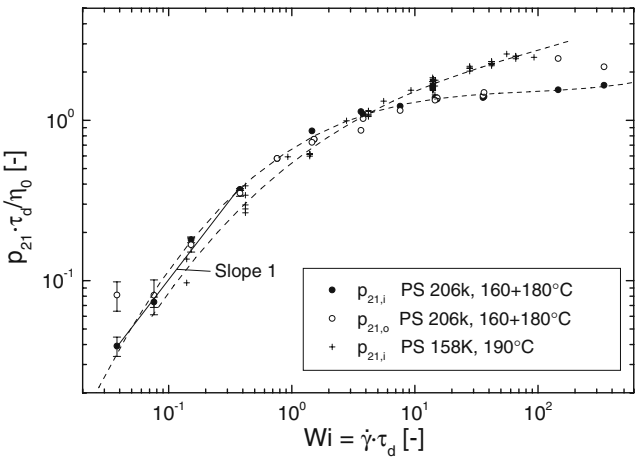

Fig. 15 Steady-state shear stress p_{21}, determined from the inner disk torque (*filled circles*), and the outer ring torque (*open circles*). The stress is made dimensionless with the initial slope η_0/τ_d of the linear viscosity curve $\eta^0(t)$. The *crosses* are preliminary data for a polydisperse PS 158K (measured at 190°C, p_{21} from inner disk torque shown). The *dashed lines* are guides to the eye

stress field. The slower relaxation of N_1 compared to p_{21} is unexplained, but has also been found by Attané et al. (1985) for a PS solution with a similar number of entanglements per chain as our melt.

Under the influence of a normal force, the gap of a compliant rheometer opens, resulting in a radial flow of the melt. Therefore, conditions have been identified for the axial and torsional response times t_a and t_t. If these are fulfilled, rheological measurements will be unaffected by instrument compliance (Hansen and Nazem 1975):

$$t_t/\tau_d \ll 1 \tag{14}$$

$$t_t = \frac{20\pi\eta R^3}{3\alpha K_T} \tag{15}$$

$$t_a/\tau_d \ll 1 \tag{16}$$

In supplement, Dutcher and Venerus (2007) identified a condition for minimizing the crosstalk between the torque and normal force signal:

$$De^2\left(t_a/\tau_d\right) = (\Omega\tau_d)^2\left(t_a/\tau_d\right) = \left(\dot{\gamma}\,\alpha\tau_d\right)^2\left(t_a/\tau_d\right) \ll 1 \tag{17}$$

For the MTR 25 and some typical geometries, Eqs. 14, 16, and 17 have been evaluated in Table 6. Only the few numbers in bold do not satisfy the criteria given above. Limitations are given by small cone angles and large samples. Crosstalk is a potential problem at low temperatures (high viscosities).

Homogeneity of the flow/edge fracture

Each elastic fluid, even when subjected to laminar flow, shows elastic instabilities: the edge is warped and some monodisperse samples even escape from the rheometer gap by forming radial rolls (see Schweizer and Bardow 2006). These phenomena lead to deviations from the spherical shape, which is a prerequisite for Eqs. 2, 3, and 5 to hold. When the edge fractures, the torque and normal force signals on the outer ring will drift, either in a steady or oscillatory manner. The normal force on the inner disk will also respond, although in a lesser degree since the integral $\int_0^{R_i} p_{22}\mathrm{d}r$ is affected by the flow in the outer part of the sample as well. For the partitioned plate on the RMS 800, it was shown (Schweizer 2002, Fig. 2) that normal force oscillations due to edge fracture are seen later in the inner disk, the larger the sample, i.e., the further the fracturing edge is away from the inner disk.

With the MTR 25 method, the normal force signal F_o of the outer ring is needed for calculating N_1 and N_2 (Eqs. 4, 5, and 7). Thus, any disturbance will propagate to the calculation of the normal stresses. From the raw signals F_i and F_o, it is not possible to quantify the flow homogeneity of the inner and outer parts of the sample. For the torque, however, both torques M_i and M_o should independently lead to the same stress p_{21}. Figure 15 shows that the steady-state shear stresses calculated from Eqs. 4 and 9 do agree up to Weissenberg numbers of ≈100. Since p_{21} depends on torque as R^{-3}, this shows that the edge is not disrupted up to that rate for strains not larger than about 10–12. For larger strains, Fig. 11 shows that the outer torque can be considerably lower due to edge fracture, whereas the inner one remains constant up to strains of 20–30.

Another way to quantify inhomogeneous flow is to measure the surface velocity profile $v_x(y)$ (Schweizer and Stöckli 2008). At start, with a well-shaped rim, the

Table 6 Evaluation of Eqs. 14, 16, and 17

Temperature [°C]	Shear rate [s^{-1}]	η[Pa s]	α [rad]	R [mm]	t_a [s]	t_a/τ_d[−]	$De^2(t_a/\tau_d)$[−]
160	5	168,000	0.15	18	1.689	0.23	**6.93**
160	5	168,000	0.15	10	0.938	0.13	**3.85**
160	47.16	23,040	0.15	18	0.232	0.032	**84.57**
160	47.16	23,040	0.15	10	0.129	0.018	**46.98**
180	1	52,000	0.15	18	0.523	**0.688**	0.0089
180	1	52,000	0.15	10	0.290	0.38	0.0050
180	5	17,500	0.15	18	0.176	0.23	0.075
180	5	17,500	0.15	10	0.098	0.13	0.042
180	47.16	2,400	0.15	18	0.024	0.032	**0.9**
180	47.16	2,400	0.15	10	0.013	0.018	0.51
160	5	168,000	0.1	10	3.167	0.43	**5.78**
160	47.16	23,040	0.1	10	0.434	0.060	**70.47**
180	1	52,000	0.1	10	0.980	**1.3**	0.0074
180	5	17,500	0.1	10	0.330	0.43	0.063

Common parameters: $K_A = 10^7$ N/m, $\tau_d = 0.76$ s (at 180°C). The bold values are critical, i.e., larger than about $^1/_2$

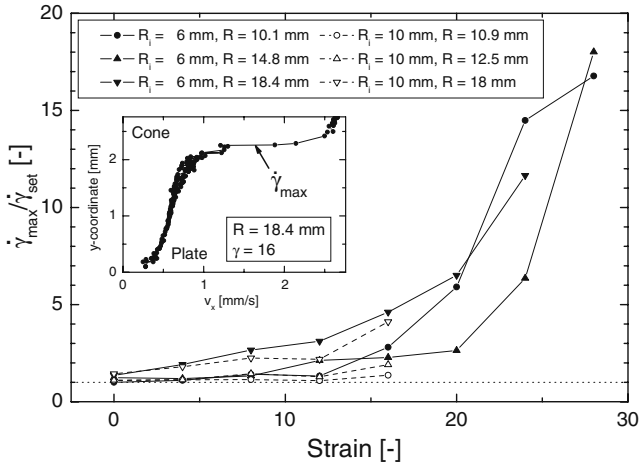

Fig. 16 Ratio of the maximum shear rate at the surface to the set one ($\dot{\gamma} = 1\,\mathrm{s}^{-1}$). The *inset* shows how the surface velocity profile determined by particle tracking looks like for the largest sample at $\gamma = 16$. Clearly, the high shear rate layer forming at $y = 2.2$ mm is seen. Due to sagging, it is not at half height of the gap

velocity profile is linear and its slope $dv_x/dy = \dot{\gamma}_{\mathrm{set}}$. Under the influence of normal stresses and slight irregularities at the surface, a transition towards shear banding occurs. The inset of Fig. 16 shows the maximum shear rate $\dot{\gamma}_{\mathrm{max}}$ at the inflection point of the velocity profile, which is in the separation layer of the (two) shear bands. If the ratio $\dot{\gamma}_{\mathrm{max}}/\dot{\gamma}_{\mathrm{set}}$ is taken as a measure for the homogeneity, Fig. 16 shows that up to strains of about 12, the velocity profile remains linear for $R < 13$ mm. This limit, determined from a rheometry-independent method, coincides with Fig. 11b, where the viscosity η_{outer} from the ring torque is constant up to $\gamma \approx 12$ and with Fig. 12b, c, where Ψ_1 and $-\Psi_2$ from the MTR 25 and the RMS 800 methods coincide up to the same strain. Beyond $\gamma \approx 12$, inhomogeneous flow and finally strong shear banding set in, forbidding any further evaluation of the data. For the largest samples with R = 18.4 mm, the velocity profile is non-linear from the beginning ($\dot{\gamma}_{\mathrm{max}}/\dot{\gamma}_{\mathrm{set}} > 1$). This is due to sagging of the bulge in the gap of 2.7 mm height and prevents shaping a spherical surface prior to start. Thus, by means of surface particle tracking and the condition ($\dot{\gamma}_{\mathrm{max}}/\dot{\gamma}_{\mathrm{set}} = 1$), the correct shape of the surface (spherical) can be verified.

Monodisperse PS melts do show departure from homogeneous flow at lower shear rates and strains than polydisperse PS. Figure 15 provides a possible explanation for this experimental finding. As can be seen, the slope $\mathrm{d}(p_{21}\cdot\tau_d/\eta_0)/\mathrm{d(Wi)}$ in the range $10 < \mathrm{Wi} < 100$ is much shallower for monodisperse PS 206k than for polydisperse PS 158K. This means that for a stress in the range of the plateau, the corresponding shear rate is ambiguous for PS 206k, which might amplify a starting irregularity at the surface. $p_{21}(\dot{\gamma})$ with even a negative slope was reported by Neergaard et al. (2000) for PS (M_w of $1.9{\cdot}10^6$, polydispersity index of 1.2) in TCP (0.135 g/cm^3). Although our PS 206k is of narrower polydispersity, it does not show the negative slope in $p_{21}(\dot{\gamma})$. GPC showed that the sample has a small foot on the high molecular weight tail of the peak. This might possibly be a reason for N_1 and $-N_2$ to rise at low shear rates ($<0.1\ \mathrm{s}^{-1}$).

Conclusions

The MTR 25 is the first rheometer for polymer melts that allows a direct determination of N_1 and N_2 from a single sample in an extended range of shear rates. The axial compliance is lower than of any other rheometer in our group. The high stiffness was realized with a specific design of the load cell with strain gauges for the signal detection. They feature a very fast response time and their supreme sensitivity allowed a very stiff design of the springs. Electric heating is a must for a constant measuring gap—a key requisite for accurate normal stress measurements. The high load experimental window is now limited entirely by the flow properties of the melt and no longer by instrumental restrictions.

The comparison of the two methods to determine N_1 and N_2 (MTR 25 method: one sample, evaluate F_i and F_o and RMS 800 method: several samples with different R, evaluate F_i) leads to the following conclusions:

- Edge fracture restricts the use of the MTR 25 method, but the partitioned plate with two load cells allows to recognize and quantify the departure from homogenous flow without particle tracking.
- The rugged construction with high normal force makes the acquisition of data for the RMS 800 method much easier, allowing quicker loading, larger samples, and higher shear rates.
- The torque from the inner disk provides viscosity data of excellent quality, long after edge fracture sets in at the rim of the sample.
- Equation 6 provides a consistency check for the RMS 800 method which can be quantified by the regression coefficient R. In the MTR 25 method, the outer torque is a normal force-independent indicator for the onset of edge fracture.
- Conditioning of the rim prior to start can postpone, but not prevent edge flow instabilities. The second normal stress difference turns out to be a very

sensitive parameter to study this in more detail in the future.
- Whether the surface is properly shaped can be verified by surface particle tracking and the condition ($\dot{\gamma}_{max}/\dot{\gamma}_{set} = 1$).
- Before edge fracture starts, the transient behavior of N_2 is better described by the MTR 25 method.
- Surface particle tracking shows that the flow becomes inhomogeneous at strains around 10. Therefore, to measure N_2 in the steady state, the RMS 800 method provides more precise data, since it only considers the normal force from the inner disk.
- There is still no method which can determine N_2 of polymer melts in the transient and the steady-state regime. With the MTR 25, however, data for both the RMS 800 and the MTR 25 methods can be provided.
- Since the curvature of the rim at start depends on the loading procedure and rest time and quickly increases during shear, it is not surprising that N_2—as a surface-related property—strongly depends on it. Keeping loading conditions strictly constant is therefore crucial for reproducible experiments.
- The η, Ψ_1, and Ψ_2 data obtained with the MTR 25 method in Fig. 9 can be time–temperature-superposed in the temperature window $160 < T < 180$°C.

The following questions remain unanswered by this study:

- The ratio $-N_2/N_1$ shows a tendency to rise at low shear rates, instead of reaching a steady state.
- $|N_2|$ determined with the RMS 800 method shows a larger overshoot at start-up and a larger undershoot after cessation than the one determined with the MTR 25 method.
- The sign change in Ψ_2 in Fig. 12f after cessation of flow is corroborated by a high correlation coefficient of $R > 0.95$ and by the data from the MTR 25 method. Surface particle tracking, however, puts it in question, as it shows strong shear banding before the flow stops.
- Although surface particle tracking, the outer torque, and N_2 show that the flow is strongly inhomogeneous (up to shear banding) beyond $\gamma = 10$, the inner torque remains constant up to strains of 20–30. A tentative explanation for this could be that the perturbations remain confined to the outer part of the sample. This is an assumption made by Venerus (2007) when he analyzed the influence of the rim shape on the normal stress differences.
- A similar enigma is that the evaluation to Eq. 6 before cessation gives correlation coefficients $R > 0.95$, although the flow is clearly inhomogeneous, as seen from η_{outer} (Fig. 11b, d) and particle tracking (Fig. 16). Again, this can only be understood, if perturbations are limited to the outer part of the sample.
- Figure 8 shows that for shear rates larger than 10 s^{-1}, $|\Psi_2|$ for some experiments shows a strong depression or even a sign change before the steady state is reached or relaxation starts. It is not clear, what the origin of that depression is. Presumably, it has to do with edge warpage for Ψ_1 of the same test is smooth and reproducible.

Acknowledgements The authors would like to thank Prof. Hans Christian Öttinger for providing from theory the motivation for N_2 measurements. The rheometer could not have been successfully built without the experience from Prof. Joachim Meissner's partitioned plate on the RMS 800, which finally proved the versatility of the technique. J.M. and Clarisse Luap are thanked for their critical comments on the paper. Frank Moszner and Moritz Küng helped to perform test measurements on the instrument. Finally, the ETH Zürich is acknowledged for funding the construction of the rheometer.

References

Adams N, Lodge AS (1964) Rheological properties of concentrated polymer solutions II. A cone-and-plate and parallel plate pressure distribution apparatus for determining normal stress differences in steady shear flow. Philos Trans R Soc Lond, A 256(1068):149–184

Attané P, Pierrard JM, Turrel G (1985) Steady and transient shear flows of polystyrene solutions II: shear-rate dependence of non-dimensional viscometric functions: characteristic relaxation times. J Non-Newton Fluid Mech 18:319–333

Dutcher CS, Venerus DC (2007) Compliance effects on the torsional flow of a viscoelastic fluid. J Non-Newton Fluid Mech 150(2–3):154–161

Fetters LJ, Lohse DJ, Graessley WW (1999) Chain dimensions and entanglement spacings in dense macromolecular systems. J Polymer Sci, Part B, Polym Phys 37:1023–1033

Hansen MG, Nazem F (1975) Transient normal force transducer response in a modified Weissenberg Rheogoniometer. Trans Soc Rheol 19(1):21–36

Jobling A, Roberts JE (1959) Flow testing of viscoelastic materials. Design and calibration of the Roberts–Weissenberg model R8 Rheogoniometer. J Polym Sci 36:421–431

Kalogrianitis SG, van Egmond JW (1997) Full tensor optical rheometry of polymer fluids. J Rheol 41(2):343–364

Kaye A, Lodge AS, Vale DG (1968) Determination of normal stress differences in steady shear flow. II. Flow birefringence, viscosity, and normal stress data for a polyisobutylene liquid. Rheol Acta 7(4):368–379

Magda JJ, Baek SG (1994) Concentrated entangled and semidilute entangled polystyrene solutions and the second normal stress difference. Polymer 35(6):1187–1194

Meissner J (1972) Modification of the Weissenberg Rheogoniometer for measurement of transient rheological properties of molten polyethylene under shear. Comparison with tensile data. J Appl Polym Sci 16:2877–2899

Meissner J, Garbella RW, Hostettler J (1989) Measuring normal stress differences in polymer melt shear flow. J Rheol 33(6):843–864

Neergaard J, Park K, Venerus DC, Schieber J (2000) Exponential shear flow of linear, entangled polymeric liquids. J Rheol 44(5):1043–1054

Ohl N, Gleissle W (1992) The second normal stress difference for pure and highly filled viscoelastic fluids. Rheol Acta 31:294–305

Pollett WFO (1955) Rheological behaviour of continuously sheared polyethylene. Br J Appl Phys 6:199–206

Schweizer T (2002) Measurement of the first and second normal stress differences in a polystyrene melt with a cone and partitioned plate tool. Rheol Acta 41:337–344

Schweizer T (2004) A quick guide to better viscosity measurements of highly viscous fluids. Appl Rheol 14(4):197–201

Schweizer T, Bardow A (2006) The role of instrument compliance in normal force measurements of polymer melts. Rheol Acta 45(4):393–402

Schweizer T, Stöckli M (2008) Departure from linear velocity profile during shear of polystyrene melts in cone–plate geometry. J Rheol 52(3):713–727

Schweizer T, van Meerveld J, Öttinger HC (2004) Nonlinear shear rheology of polystyrene melt with narrow molecular weight distribution—experiment and theory. J Rheol 48(6):1345–1363

Venerus DC (2007) Free surface effects on normal stress measurements in cone and plate flow. Appl Rheol 17:36494-1–36494-6

Winter HH (1997) Analysis of dynamic mechanical data: inversion into a relaxation time spectrum and consistency check. J Non-Newton Fluid Mech 68:225–239